Asian Journal of Pharmaceutical Sciences 18 (2023) 100874

Available online at www.sciencedirect.com

ScienceDirect

journal homepage: www.elsevier.com/locate/AJPS

Research Article

Mechanistic engineering of celastrol liposomes induces ferroptosis and apoptosis by directly targeting VDAC2 in hepatocellular carcinoma

Piao Luo[a,1], *Qian Zhang*[a,1], *Shuo Shen*[b,1], *Yehai An*[a], *Lixia Yuan*[a], *Yin-Kwan Wong*[c], *Sizhe Huang*[a], *Shaohui Huang*[a], *Jingnan Huang*[d], *Guangqing Cheng*[b], *Jiahang Tian*[a], *Yu Chen*[a], *Xiaoyong Zhang*[a], *Weiguang Li*[e,*], *Songqi He*[a,*], *Jigang Wang*[a,b,d,f,g,*], *Qingfeng Du*[a,*]

[a] *School of Traditional Chinese Medicine and School of Pharmaceutical Sciences, Southern Medical University, Guangzhou 510515, China*
[b] *State Key Laboratory for Quality Ensurance and Sustainable Use of Dao-di Herbs, Artemisinin Research Center, and Institute of Chinese Materia Medica, China Academy of Chinese Medical Sciences, Beijing 100700, China*
[c] *Department of Biological Sciences, National University of Singapore, Singapore 117543, Singapore*
[d] *Department of Nephrology, Shenzhen key Laboratory of Kidney Diseases, and Shenzhen Clinical Research Centre for Geriatrics, Shenzhen People's Hospital, The First Affiliated Hospital, Southern University of Science and Technology, Shenzhen 518020, China*
[e] *Department of Health Technology and Informatics, The Hong Kong Polytechnic University, Hong Kong 100872, China*
[f] *Department of Oncology, the Affiliated Hospital of Southwest Medical University, Luzhou 646000, China*
[g] *National Pharmaceutical Engineering Center for Solid Preparation of Chinese Herbal Medicine, Jiangxi University of Chinese Medicine, Nanchang 330006, China*

ARTICLE INFO

Article history:
Received 1 July 2023
Revised 20 October 2023
Accepted 8 November 2023
Available online 30 November 2023

Keywords:
Celastrol
VDAC2
Ferroptosis
Apoptosis
Hepatocellular carcinoma
Liposomes

ABSTRACT

Hepatocellular carcinoma (HCC) is one of most common and deadliest malignancies. Celastrol (Cel), a natural product derived from the *Tripterygium wilfordii* plant, has been extensively researched for its potential effectiveness in fighting cancer. However, its clinical application has been hindered by the unclear mechanism of action. Here, we used chemical proteomics to identify the direct targets of Cel and enhanced its targetability and anti-tumor capacity by developing a Cel-based liposomes in HCC. We demonstrated that Cel selectively targets the voltage-dependent anion channel 2 (VDAC2). Cel directly binds to the cysteine residues of VDAC2, and induces cytochrome C release via dysregulating VDAC2-mediated mitochondrial permeability transition pore (mPTP) function. We further found that Cel induces ROS-mediated ferroptosis and apoptosis in HCC cells. Moreover, coencapsulation of Cel into alkyl glucoside-modified liposomes (AGCL) improved its antitumor efficacy and minimized its side effects. AGCL has been shown to effectively suppress the proliferation of tumor cells. In a xenograft nude mice experiment, AGCL significantly inhibited tumor growth and promoted apoptosis. Our findings reveal that

* Corresponding authors.
E-mail addresses: weiguang.li@polyu.edu.hk (W. Li), hesongqijz@126.com (S. He), jgwang@icmm.ac.cn (J. Wang), dqf1689@smu.edu.cn (Q. Du).
[1] These authors contributed equally to this work.
Peer review under responsibility of Shenyang Pharmaceutical University.

https://doi.org/10.1016/j.ajps.2023.100874

Cel directly targets VDAC2 to induce mitochondria-dependent cell death, while the Cel liposomes enhance its targetability and reduces side effects. Overall, Cel shows promise as a therapeutic agent for HCC.

1. Introduction

Cell death is an indispensable part of the cell life process and the self-regulation of living organisms. It is also a critical process in diverse aspects of tumor development, homeostasis, as well as treatment. Numerous different types of programmed cell death (PCD) have been defined with each possessing unique molecular and cellular mechanisms. Among them are several types of PCD that are closely related to mitochondrial dysfunction such as ferroptosis, mitochondrial apoptosis and mitophagy in cancers [1,2]. This is mainly due to the fact that mitochondria can drive aberrant cancer cell aerobic glycolysis, to acquire energy, and regulates redox homeostasis, biogenesis and mitochondrial tricarboxylic acid cycle in cancers. Thus, mitochondria play a multifunctional and crucial role in the development and progression of malignant tumor, and developing drugs that target mitochondria will be a new strategy to treat tumors. Emerging studies have proposed the induction of mitochondria-dependent cell death as a new form of treatment for different cancers, including liver cancer, pancreatic cancer, and malignant melanoma [3–5]. Moreover, most notably in hepatocellular carcinoma (HCC), disruption of iron homeostasis and mitochondrial damage have been reported to enhance radiosensitivity and trigger ferroptosis and apoptosis to destroy cancer cells [6–8]. These studies have attempted to overcome multidrug resistance by developing approaches to induce mitochondria-dependent cancer cell death.

Voltage-dependent anion channel (VDAC) is known as the mitochondrial porin, located at mitochondrial outer membranes, which control the transmembrane transport of numerous ions and metabolites [9]. By regulating molecular exchange between the cytosol and mitochondria, VDAC's key function is transporting metabolites and other essential molecules. Additionally, VDAC has been shown to play a role in triggering apoptosis, or PCD, in certain conditions, and is implicated in a variety of diseases including cancers [10]. Erastin (ERA), a ferroptosis activator, alters the permeability of the outer mitochondrial membrane and induces ferroptosis via binding directly to VDAC2/3 in tumor cells [11], which suggests that the VDAC2/3 protein participates in triggering ferroptotic cell death. ERA also facilitates radiotherapy and chemotherapy in the treatment of cancers [12]. Moreover, VDACs have also been regarded as a key protein of mPTP for mitochondria-mediated apoptotic pathway, facilitating the influx of pro-apoptotic members from mitochondria into the cytosol through mitochondrial pore channels [13]. The opening of VDACs has been reported to promote ROS generation, and mitochondrial damage in cancer cells [14]. Therefore, identifying potent and selective inhibitors of mPTP may provide novel candidates for cancer therapy.

Celastrol (Cel) is a natural triterpenoid compound derived from *Tripterygium wilfordii* herb [15]. Cel has been reported to exhibit multiple biological activities, including suppressing the proliferation and growth of colorectal cancer, melanoma, gastric cancer and prostate cancer [16,17]. Further investigation has revealed that Cel induces ROS-mediated mitochondrial apoptosis and cell death in cancer cells [16]. However, the exact molecular mechanism of Cel-induced mitochondria-dependent cell death remains poorly understood. At the same time, the severe side effects caused by Cel represent a major barrier to any possible clinical application [18].

Herein, we report for the first time that Cel is a novel covalent inhibitor of VDAC2. It is reported that targeting VDAC2 triggers mitochondrial apoptosis or ferroptosis in human cancer cells [11,19]. Increasing evidence indicated that nano-delivery system of ferroptosis-induced anticancer was widely studied in cancer treatment [20,21]. In this study, our data showed that Cel notably inhibited the growth and proliferation of human liver cancer cells. We identified VDAC2 as a mitochondrial Cel binding protein, and further revealed that Cel could directly bind to the cysteine residues of VDAC2. Further study demonstrated that Cel damages VDAC2 channels located at the mitochondrial outer membrane to trigger the release of cytochrome C (Cyto C). In a domino effect, this further results in ROS generation, cellular dysfunction, and ion dyshomeostasis, ultimately inducing ROS-mediated mitochondrial apoptosis or ferroptosis in liver cancer cells. Moreover, we developed a method of coencapsulating Cel into alkyl glucoside-modified liposomes (AGCL). The formulation of the liposomes was based on alkyl glucose and the glucose structural fragments were modified into the membrane structure of liposomes. AGCL could effectively be recognized by the glucose transporters (GLUT1) of tumor cells [22]. As a result, the anti-tumor effect of Cel had been improved and its side effects on normal tissues had been reduced.

Overall, our research findings provide evidence that VDAC2 acts as a direct effector for Cel-mediated cancer cell death. Thus, we propose that this protein serves as a molecular mechanism for the anti-tumor activity of Cel, while we have demonstrated that a nano-formulation of Cel enhances its targetability and reduces its side effects.

2. Materials and methods

2.1. *Reagents and materials*

Celastrol (Cel, over 98% purity) was from Shanghai yuanye Bio-Technology Co., Ltd (Shanghai, China). N-acetylcysteine (NAC),

erastin (ERA) and deferoxamine (DFO) were procured from AbMole BioScience. The following chemicals were used in the click chemistry reaction and LC-MS/MS reagents: TAMRA-azide (Sigma, USA), NaVc (Sigma, USA), $CuSO_4$ (Sigma, USA) and Biotin-azide (Sigma, USA), THPTA (ClickChemistryTools), TMT 10 plex reagent, high capacity neutravidin agarose resin and TEAB (Thermo Fisher, USA). Liposomes materials: cholesterol, soy bean phospholipid (SC95), DSPE-mPEG2000 and FITC-PEG-DSPE were obtained from Shanghai A.V.T. Pharmaceutical Co., Ltd (Shanghai, China). N-octyl β-D-glucopyranoside was procured from Yuanye Bio-Technology Co., Ltd (Shanghai, China). Anhydrous ethanol and acetonitrile HPLC grade were purchased from Tianjin Concord Technology Co., Ltd (Tianjin, China). Moreover, specific primary antibodies: anti-VDAC2 (ab154856), anti-Cyto C (ab133504), anti-Bad (ab32445) and anti-Caspase-3 (ab184787) were purchased from Abcam (Shanghai, China). Anti-Ki-67 was procured from proteintech (Chicago, USA). β-actin antibody was purchased from Affinity Biosciences (OH, USA). Human hepatoma cell lines including SK-Hep1, HepG2 and H22 cells were procured from the Chinese Academy of Medical Sciences (Beijing, China). The experimental animals used were sourced from Vital River Laboratory Animal Technology (Beijing, China). Animal experiments were approved by the China Animal Care and Use Committee (Aup-210320-WJG-001-01).

2.2. *Cell viability assay*

The Cell Counting Kit-8 (CCK-8) assay (Beyotime, China) was performed to measure the viabilities of SK-Hep1 or HepG2 cells that were incubated with serial dilutions of Cel, Cel-P or Cel liposomes (dilution from 20 μM equal ratios to 0) for 24 or 48 h, following the manufacturer's protocol. After incubation, the reagent (The ratio of CCK-8 reagent to medium was 1:10) was added for 1 h, and absorbance was detected using a multimode plate reader (EnVision2105, PerkinElmer, USA).

2.3. *In situ fluorescence labeling experiments*

SK-Hep1 or HepG2 cells were cultured in six-well plates until they reached 80%−90% confluence. After incubation with Cel-P (2 μM) for 3–4 h with or without pre-treatment with excess Cel (4 μM) for 1 h, cells were collected (1,000 rpm, 4 °C, 5 min), and then cells were broken by ultrasound with RIPA (Thermo, USA) buffer with protease inhibitor cocktail. Finally, the soluble protein is obtained by centrifugation (14,000 rpm, 4 °C, 10 min). A soluble protein solution was reacted with a click chemistry cocktail containing NaVc (1 mM), THPTA (100 μM), $CuSO_4$ (1 mM) and TAMRA-N_3 (50 μM) for 2–4 h. The labeled proteins were precipitated by pre-chilled acetone and collected by centrifugation for 12–15 min (14,000 rpm, 4 °C) and air-dried. The protein was dissolved in loading buffer and heated (95 °C, 15 min), followed by 10 % SDS-PAGE electrophoresis (80 V 40 min, followed by 120 V 120 min) and fluorescence scanning in laser scanner (Azure Biosystems Sapphire, Azure Biosystems, USA). Coomassie brilliant blue (CBB) (Thermo, USA) staining was used as a loading control.

For recombinant human protein labeling, recombinant protein was treated with probe or pre-incubated with excessive Cel, and then reacted with click chemistry cocktail. Proteins were separated by SDS-PAGE and visualized as previously described. For competitive assay, protein was pre-incubated with Cel for 1–2 h, and then processed as previously described.

2.4. *Identification of targets and pull down assay*

The general procedures were similar to those previously described [23,24]. SK-Hep 1 or HepG2 cells were cultured until 80%−90% confluence. Sample was first pre-incubated with Cel and then treated with 2 μM Cel-P. Cells were then collected and lysed. Equal amounts of proteins were used for the click reaction. Proteins after acetone-precipitation were dissolved in PBS containing 1.5% SDS (sodium dodecyl sulfate), and then diluted in 0.1% SDS. After incubating the streptavidin beads, a sequential wash was performed using 1% SDS, 0.1% SDS and 6 M urea.

In-gel digestion was performed by excising the band of interest (25–35 kDa) which was cut into small particles. The particles were then washed with 25 mM ammonium bicarbonate buffer (ABB) or 50% acetonitrile in 25 mM ABB buffer, and subsequently dehydrated. Reduction and alkylation of the gel particles were achieved using 10 mM DTT or 50 mM IAA. The samples were then digested with 1–2 μg trypsin overnight at 37 °C. The resulting peptides were labeled using TMT regents and subsequently analyzed through LC-MS/MS (Thermo fisher scientific, Orbitrap Eclipse™ Tribrid™, USA).

For pull down-Western blotting, the enriched protein was eluted from beads by incubation with loading buffer at 95 °C for 10 min. The supernatant was then obtained through centrifugation for 10 min, followed by usage in Western blotting procedures.

2.5. *Cellular imaging*

Cells were seeded in four-chamber glass bottom dishes, then incubated with Cel-P (1 μM) for 1 h. After an incubation period of 3 h, the medium was removed, and cells were gently washed with cold PBS. Subsequently, cells were fixed, washed and permeabilized. Cells were then incubated with click chemistry cocktail for 2–4 h at RT. For co-localization experiments with target protein, cells were further treated with anti-VDAC2 (1:2,000 ratio) overnight at 4 °C, and then treated with a fluorescent secondary antibody and Hoechst 33342. Images were acquired using a confocal fluorescence microscope (Leica TCS SP8 SR, Germany) and analyzed by an ImageJ software.

2.6. *Cellular thermal shift assay (CETSA)*

SK-Hep 1 or HepG2 cells lysis (2–3 mg/ml) were treated with Cel or DMSO for 1–2 h. 50 μl of each cell suspension was dispensed into 10 PCR tubes and heated at the different temperatures (starting temperature 4 °C) from 37 °C to 73 °C by a thermal cycle for 3 min using applied biosystems PCR analyzer (Thermo fisher scientific, USA). The supernatant was obtained through centrifugation, and analyzed by Western blotting analysis.

2.7. Plasmids constructs and purification of recombinant proteins

Human VDAC2 gene was subcloned into pCold I vector (Sangon, Shanghai, China) to generate a 6 × His-tagged fusion protein. To obtain cysteine-mutated VDAC2 proteins (Cys13 to Ser13), plasmids with site-mutants gene subcloned into pCold I vector were constructed by Sangon. The *E. coli* strain BL21 was transformed with plasmids for proteins purification in LB medium supplemented with 100 μg/ml ampicillin, and then the bacteria were cooled for 30 min at 4 °C prior to before adding 1 mM IPTG. Bacteria's protein was extracted in lysis buffer (150 mM NaCl, 20 mM Tris–HCl, protease inhibitor cocktail). Subsequently, samples were centrifugated to acquire supernatant, following by Ni-NTA beads column (QIAGENQiagen, USA) to purify recombinant protein by using binding buffer (150 mM NaCl, 20 mM Tris–HCl) with Imidazole. The purity of recombinant protein was assessed by CBB after 10% SDS-PAGE gel separation.

2.8. Molecular docking

The crystal structure of VDAC2 protein was obtained from AlphaFold Protein Structure Database (ID: AF-P45880-F1). Molecular docking was performed to obtain the optimized binding conformation of the VDAC2-Cel system using the Autodock vina software (version 1.5.6). The optimized conformation was picked out based on the docking scores. Moreover, Pyrx-0.8 and Pymol software were also employed for molecular docking and mapping.

2.9. UV–visible spectra assay

UV-visible spectra of Cel was detected at 300–600 nm using a multimode 96-well plate reader in PBS buffer. Cel (100 μM) was treated with the specific proteins (20 μM) or GSH (1 mM), and the absorbance of its spectra was recorded.

2.10. Mitochondrial function and fluorescence imaging

The co-localization experiments of Cel-P with mitochondria required cell seeding in 4-chamber glass bottom dishes, followed by treatment with Cel-P. After an incubation of 3 h, the medium was removed, and washed with PBS. Subsequently, cells were further incubated with Mito-Tracker Red (200 nM, Thermo fisher scientific, USA), and cells were and fixed, gently washed, and then permeabilized. Samples were incubated with click chemistry cocktail for 2–4 h at RT. Images were acquired with fluorescence microscopy.

The mitochondrial membrane potential (MMP) was ascertained through the utilization of MitoScreen kit (NO:551,302, JC-1 staining) provided by BD Biosciences. The MMP of Cel-treated cancer cells was evaluated based on the ratio of red to green fluorescence intensity. Moreover, for the release of Cyto C to evaluate mitochondrial function, cells were further treated with Mito-Tracker Red, incubated with anti-Cyto C, and then treated with fluorescent secondary antibody and Hoechst 33342. Images were acquired with fluorescence microscopy.

2.11. Western blotting

Cells were collected and lysed in RIPA buffer. Protein samples were separated on SDS-PAGE gel and transferred to PVDF membrane. After blocking nonspecific binding with 5% BSA, the membrane was immunoblotted with anti-VDAC2, anti-Cyto C, anti-Bad, anti-Caspase-3 and β-actin overnight at 4 °C, followed by incubation with secondary antibody. The protein band was detected using the Enhanced Chemiluminescence (ECL) (Azure C400, USA).

2.12. Reactive oxygen species (ROS) analysis

Intracellular ROS was measured by incubating cells with Cel (1 μM) for 12 h, followed by incubation with the DCFH-DA fluorescent probe (S0033, Beyotime, China) according to the manufacturer's protocol. Fluorescence intensity was determined using flow cytometric analysis or confocal microscopy.

2.13. Lipid peroxidation (LPO), iron ion and glutathione (GSH) assessment

LPO (A106–1–2), GSH (A006–2–1) and iron ion assay kit (A039–2–1) were obtained from Jiancheng Bioengineering Institute (Nanjing, China). These kits were used to detect intracellular content of corresponding index in cancer cells with or without Cel.

2.14. Colony formation assay

SK-Hep1 or HepG2 cells were seeded into 12-well plates, followed by treatment with the appropriate Cel (0.5 μM) for 24 h. The growth medium of cells was refreshed every 3 d After 12 d, cells were fixed in 4% paraformaldehyde and stained with a crystal violet solution (HT90132–1 L, Sigma-Aldrich, MO, USA) and images of colonies were taken by microscopy.

2.15. Whole-proteomic analysis

Cells treated with Cel were collected and lysed with RIPA containing 1% cocktail buffer. the protein concentration of sample was measured using BCA kit. Next, for reduction and alkylation of proteins, 5 mM DTT and 20 mM IAA were added for 30 min. The samples were finally digested overnight with trypsin at 37 °C and desalted with a commercial C_{18} column (Waters, USA), and then analyzed by LC-MS/MS.

2.16. Differentially expressed protein (DEP) and gene ontology (GO) analysis

DEP between the control (DMSO) and Cel groups was analyzed according to the abundance intensity of the two groups, which was performed by employing the "limma" package. P values were adjusted utilizing Benjamini-Hochberg (BH) method. DEPs were selected based on the absolute fold change $\geq$ 1.5 and adjusted *P* value of $<$ 0.05. Volcano plots were generated by the "ggplo2" package. Furthermore, GO analysis

was performed using the "clusterprofiler" package depending on selected DEPs.

2.17. RNA interference and transfection

The primer sequences for the small interfering RNAs (siRNAs) were designed and synthesized by RiboBio Biotechnology Co., LTD (Guangzhou, China). (Table S1). HepG2 cells were 70%–90% confluent at transfection. VDAC2 siRNA or negative control (NC) vectors and lipofectamine 3000 were diluted in Opti-MEM® Medium, respectively (Invitrogen, Carlsbad, CA), then vectors merged with lipofectamine 3000 reagent (1:1 ratio) according to the manufacturer's instructions. Finally, the efficiency was determined by Western blot.

2.18. Design of CEL liposomes with or without alkyl N-octyl-β-D-glucopyranoside

2.18.1. Preparation of AGCL or CL

The formulation of AGCL was based on alkyl glucose and the glucose structural fragments were modified into the membrane structure of liposomes. Liposomes with this structural feature could effectively be recognized by GLUT1 of tumor cells. The thin film dispersion method was used to prepare AGCL. The preparation steps and methods were as follows: dissolution, hydration, ultrasonication and filtration [22]. (1) 21.6 mg Cel, 240 mg SC95, 9 mg cholesterol, 28 mg DSPE-mPEG2000 and 26 mg N-octyl-β-D-glucopyranoside were placed into 50 ml round bottom flask, the flask was filled with 15 ml of anhydrous ethanol to completely dissolve all the ingredients. But CL didn't contain N-octyl-β-D-glucopyranoside. (2) A rotary evaporator (RE301, YAMATO, Japan) was used to evaporate anhydrous ethanol under reduced pressure at 50 °C, after that 23.6 ml purified water was added and the solute film was hydrated for 25 min to obtain the primary Cel liposomes solution. (3) The primary liposomes solution was treated with 450 w ultrasound for 2 min. (4) The primary liposomes were filtered by 0.22 μm membrane to obtain the AGCL.

2.18.2. Preparation of FAGCL, FCL and DAGCL

To assess the cellular uptake and systemic distribution of AGCL or CL, we prepared FITC fluorescent-labeled liposomes (FITC Alkyl-Glu-Cel-LS, FAGCL), FITC fluorescent-labeled liposomes (FITC Cel-LS, FCL) and DiR fluorescent-labeled liposomes (DiR Alkyl-Glu-Cel-LS, DAGCL). The preparation methods of FAGCL and DAGCL. The difference between the two preparation methods was that FITC or DiR probe needed to be added into the ethanol solution of excipients when preparing FAGCL or DAGCL. Other preparation methods of FAGCL or DAGCL were the same as preparation of AGCL.

2.19. Characterization of AGCL

2.19.1. Particle size, polydispersity index (PDI) and zeta potential

The Malvern Zetasizer Nano ZS (Malrvern Instruments, UK) was used for characterizing the parameters of AGCL. Measurements of particle size, PDI and zeta potential were performed with a helium–neon laser of 633 nm at 25 °C. Zeta potential was measured with DTS1070 sample cell, particle size and PDI were measured with DTS0012 sample cell. These data were obtained through three parallel tests for analysis. The morphology of AGCL was examined by Transmission Electron Microscope (TEM) (Hitachi, H-7650, Japan).

2.19.2. Cel content and release from AGCL

In the determination of encapsulation efficiency and drug release study, the Cel content was detected by Waters E2965 high performance liquid chromatography (HPLC). The HPLC conditions were as follows, chromatographic column used a TC–C_{18} 250 × 4.6 mm 5 μm (Agilent, USA); column temperature was set at 30 °C; the mobile phase was composed of acetonitrile-water (0.1% phosphoric acid) in a ratio of 80:20 (v/v); fow rate: 1.0 ml/min; the detection wavelength was 425 nm and the samples were kept at constant temperature of 20 °C; injection volume: 40 μl.

AGCL was loaded into dialysis bag (MWCO: 7000 Da, width: 25 mm) which was placed in 200 ml of a release solution (30% ethanol, containing 0.5% ween 80) for drug release study. Release samples were taken at 2, 4, 6, 8, 10, 12, 14, 24, 36, 48, 60 and 72 h post the initiation of the experiment. HPLC was employed to quantify the amount of Cel in the release solution and the cumulative release rate was calculated.

2.19.3. Entrapment efficiency (EE) of AGCL

The ultrafiltration method was used to determine the encapsulation rate of AGCL. The specific operation steps as follows [25]: AGCL was added into a 4 ml ultrafiltration tube, and this tube was then centrifuged at 4 °C for 2 h at a centrifugal speed of 5,000 rpm. The ultrafiltrate was transferred into a 25 ml volumetric flask, and methanol was added to the constant volume and the solution was shaken well. The Cel in volumetric flask was quantified by HPLC and the content of free Cel (Mf) was obtained. Equivalent volume of AGCL was added into the 25 ml volumetric flask, and an appropriate amount of methanol was added. After sonication for 15 min, methanol was added to the volumetric flask scale line when the flask temperature dropped to room temperature and the solution was shaked well. The Cel in liposomes solution (AGCL) was quantified by HPLC and the content (Mc) of Cel in liposomes solution (AGCL) was obtained. Mc is the total content of Cel encapsulated in liposomes and Cel not encapsulated in liposomes.

$$EE(\%) = (Mc - Mf)/Mc \times 100\%.$$

2.19.4. Differential scanning calorimetry (DSC)

The phase transition temperature of AGCL was measured using a DSC (Nano DSC, TA, USA). The test conditions were as follows: purified water was used as reference solution; before the experiment, the sample and reference liquid were degassed at a vacuum of 15 inches Hg for 10 min at 25 °C; the sample chamber pressure was set to 3 atmospheres; the heating range and heating rate were 20–110 °C and 1 °C/min, respectively.

2.19.5. *X-ray diffraction (XRD)*
AGCL were freeze-dried using a freeze dryer. Furthermore, XRD of freeze-dried AGCL was obtained by X-ray diffractometer (D8 ADVANCE, Bruker, Germany) over the range of 5 – 70° (2θ) in increments of 4°/min at 40 kV and 40 mA using Co-Kα(1.79026 Å).

2.19.6. *Fourier transform infrared spectroscopy (FTIR)*
AGCL were freeze-dried using a freeze dryer. Furthermore, the FTIR spectrum of freeze-dried AGCL was obtained by FTIR spectrometer (iS10, Nicolet, USA). The spectrums were recorded in the range of 400–4000 cm^{-1} with 32 scans. The spectrometer had a resolution of 4 cm^{-1} and a signal-to-noise ratio of 50,000:1.

2.19.7. *Stability study of AGCL*
The AGCL were prepared according to the described method above. The AGCL were sealed in a vial and stored in a refrigerator at 4 °C. After the preparation of the AGCL at the 0, 1, 2, 4 and 6 weeks, the particle size, PDI and zeta potential of AGCL were measured according to the previously described methods to evaluate the stability of the AGCL.

2.20. *Targeting evaluation in vivo and cellular uptake in vitro*

Male BALB/c mice, six weeks old, were procured from Vital River (Beijing, China). A tumor-bearing mice model of H22 cell was established, based on a previous study [26]. Intraperitoneal administration of DAGCL (the liposomes equivalent to 1 mg/kg Cel) was done after 7 d The tumor-bearing mice anesthetized with isoflurane were monitored for DAGCL fluorescence using an *In Vivo* Xtreme Imaging System (Bruker, USA) at predefined intervals of 3, 6, 12, 24, 48 and 72 h after injection. Eventually, mice were euthanized, and the tumors and relevant organs were collected for fluorescence measurement. For *in vitro* uptake assays, HepG2 cells were seeded in four-chamber glass bottom dishes, and FAGCL or FCL treatment of the cells was done at predefined intervals of 0, 1, 3, 6 and 12 h. Intracellular uptake of FAGCL or FCL was evaluated by using confocal fluorescence microscopy (Leica TCS SP8 SR, Germany) to detect fluorescent intensity.

2.21. *Xenograft tumor model*

Male BALB/c nude mice, six weeks old, were procured from Vital River (Beijing, China). For the tumor xenograft assay, SK-Hep1 cells were suspended in 200 µl PBS, and then subcutaneously injected into the right flank of the mice. After 7 d, the mice with tumor were randomly assigned to one of three groups and administered either Cel (1 mg/kg) or AGCL (the liposomes equivalent to 1 mg/kg Cel) intraperitoneally once daily for 5 d each week when the tumors grew up to around 50 mm^3. Following a two-week period, mice were euthanized, followed by serum collection to evaluate hepatic and renal function through examination of alanine aminotransferase (ALT), aspartate aminotransferase (AST), urea (UREA), creatinine (CRE) and lactate dehydrogenase (LDH). Subsequently, the lung, heart, kidney, liver, and spleen were obtained and fixed in 4 % formaldehyde to enable Hematoxylin and eosin (H&E) staining. Images were acquired by brightfield light microscope. Meanwhile, tumor apoptosis and proliferation were investigated by immumohistochemical staining assay in tumor sections.

2.22. *Statistical analysis*

Statistical significance was analyzed by using GraphPad Prism Software. Data are presented as mean ± standard deviation (SD) with at least 3 replicates. The statistical analyses included student's *t*-test and one-way ANOVA. For a statistically significant difference, the significance threshold was set as $P < 0.05$.

3. Results and discussion

3.1. *Identification of VDAC2 as a direct target of Cel by ABPP approach*

Cel is a pentacyclic triterpene derivative from *Tripterygium* genus that has been applied to treat a variety of diseases in traditional Chinese medicine (Fig. 1A). There is accumulating evidence demonstrating that Cel is a hepatoprotective agent for multiple liver diseases including HCC [27,28]. In addition, previous study found that Cel exerts anti-fibrosis effect by inducing ferroptosis of activated hepatic stellate cells [23]. To identify and explore the direct targets of Cel, Cel-probe (Cel-P) with an alkyne-tag was chemically synthesized (Fig. 1A). Cytotoxicity assays showed that Cel effectively suppressed the proliferation of SK-hep1 and HepG2 cells (Fig. 1B and S1A-S1B). Cel-P had a similar killing effect on both HCC cell lines as Cel (Fig. 1B andS1A-S1B), indicating that the additional alkyne tag had almost no influence on the cytotoxicity of Cel.

Activity-based protein profiling (ABPP) has frequently been applied to identify direct targets of natural products and drugs [29]. In particular, isobaric chemical tags (e.g., TMT and iTRAQ) have been employed to identify target proteins of bioactive small molecules in combination with ABPP [30]. Therefore, we used Cel-P to fish for the cellular target proteins of Cel through a tandem mass tag (TMT)-ABPP strategy (Fig. 1C). First, we applied Cel-P to label HepG2 and SK-hep1 cells *in situ*, after which Cel-P binding proteins were detected by a click reaction to attach a fluorescent tag (Fig. 1D and S1C). A competition assay was performed to examine whether Cel competed away Cel-P binding proteins, and results indicated that a specific band of Cel-P binding protein in the range of 25 to 35 kDa was significantly competed out by excess Cel (Fig. 1E and S1D). Next, after pull-down assay, this protein band was identified by TMT labeling and liquid chromatography-coupled tandem mass spectrometry (LC-MS/MS) quantification. MS data showed that the quantified TMT tag ratio (Cel-P/Comp) of VDAC2 protein was the highest in HepG2 cells (Fig. 1F) and among the highest in SK-Hep1 cells (Fig. S1E). In addition, we used the alkyne tag in Cel-P for performing a fluorescent imaging experiment to investigate its subcellular localization, finding that it is primarily present in the nucleus and cytoplasm in SK-Hep1 cells (Fig. S1F).

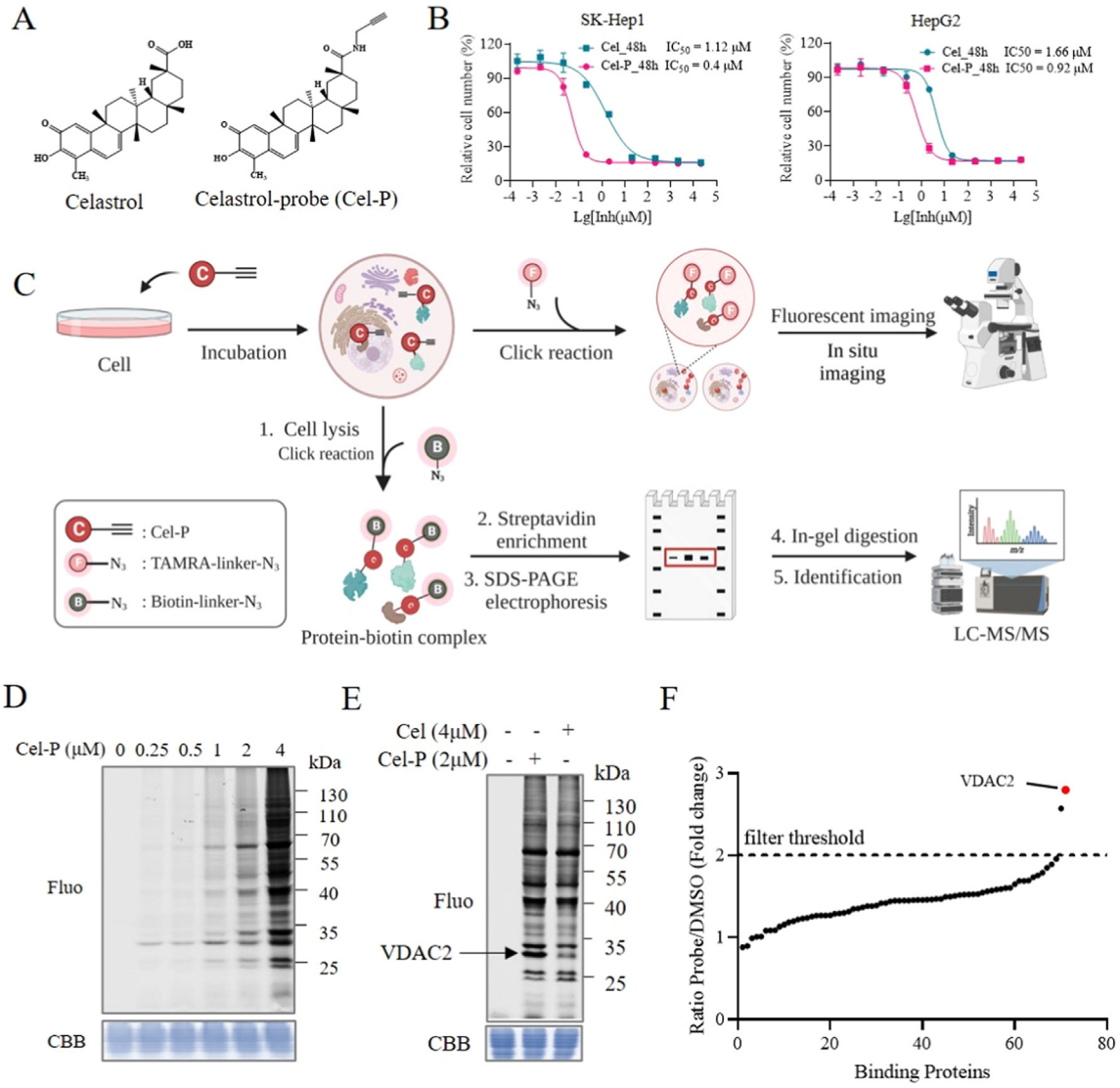

Fig. 1 – Identification of VDAC2 as a underlying target of celastrol. (A) Small molecular structures of celastrol (Cel) and celastrol-probe (Cel-P). (B) CCK-8 assay to measure viability of SK-hep1 and Hepg2 cells by Cel and Cel-P for 48 h ($n = 3$). (C) Common workflows of the TMT-ABPP experiments to identify and profile potential celastrol-targets *in situ*. (D) Potential target proteins labelling with Cel-P in HepG2 cells *in situ*. (E) VDAC2 protein with Cel-P was competed out by excess Cel in HepG2 cells *in situ*. (F) The TMT Cel-P/Comp group ratio was quantified by a competitive experiment in HepG2 cells *in situ*; the threshold of fold change (FC) ratio is defined as 2.

Furthermore, we identified two other members of the VDAC family, VDAC1 and VDAC3, in both HCC cell lines. High mobility group protein B1, pyrroline-5-carboxylate reductase 1 and other proteins were also identified in SK-Hep1 cells. We have previously reported that celestrol targets HMGB1 to improve the inflammatory response in cerebral ischemia-reperfusion [31]. Our data indicated that the quantified TMT ratio (fold change, FC) of VDAC2 was higher in both HCC cell lines (Fig. 1F). There is increasing evidence of VDAC2 functioning as a key crucial target protein for treating various cancers and developing drug [3,32]. Here, our results suggest that VDAC2 could serve as a critical target for anti-tumor activities of Cel, but this needs to be further confirmed.

3.2. *Cel directly modifies to the cysteine residues of VDAC2 by the electrophilic quinone methide moiety*

To dissect the direct interaction mechanism of Cel with VDAC2, we conducted a fluorescence staining experiment to investigate the co-localization pattern between Cel-P and VDAC2 in HepG2 cells (Fig. 2A). We further performed pull-down experiments with competition by pre-treatment with unmodified Cel. As expected, Cel-P effectively pulled down VDAC2 protein, while pre-treatment with excess Cel competed this interaction away (Fig. 2B). In addition, we carried out a cellular thermal shift assay (CETSA), a method to detect interactions between small molecule drugs or compounds and proteins by assaying the thermal stability of

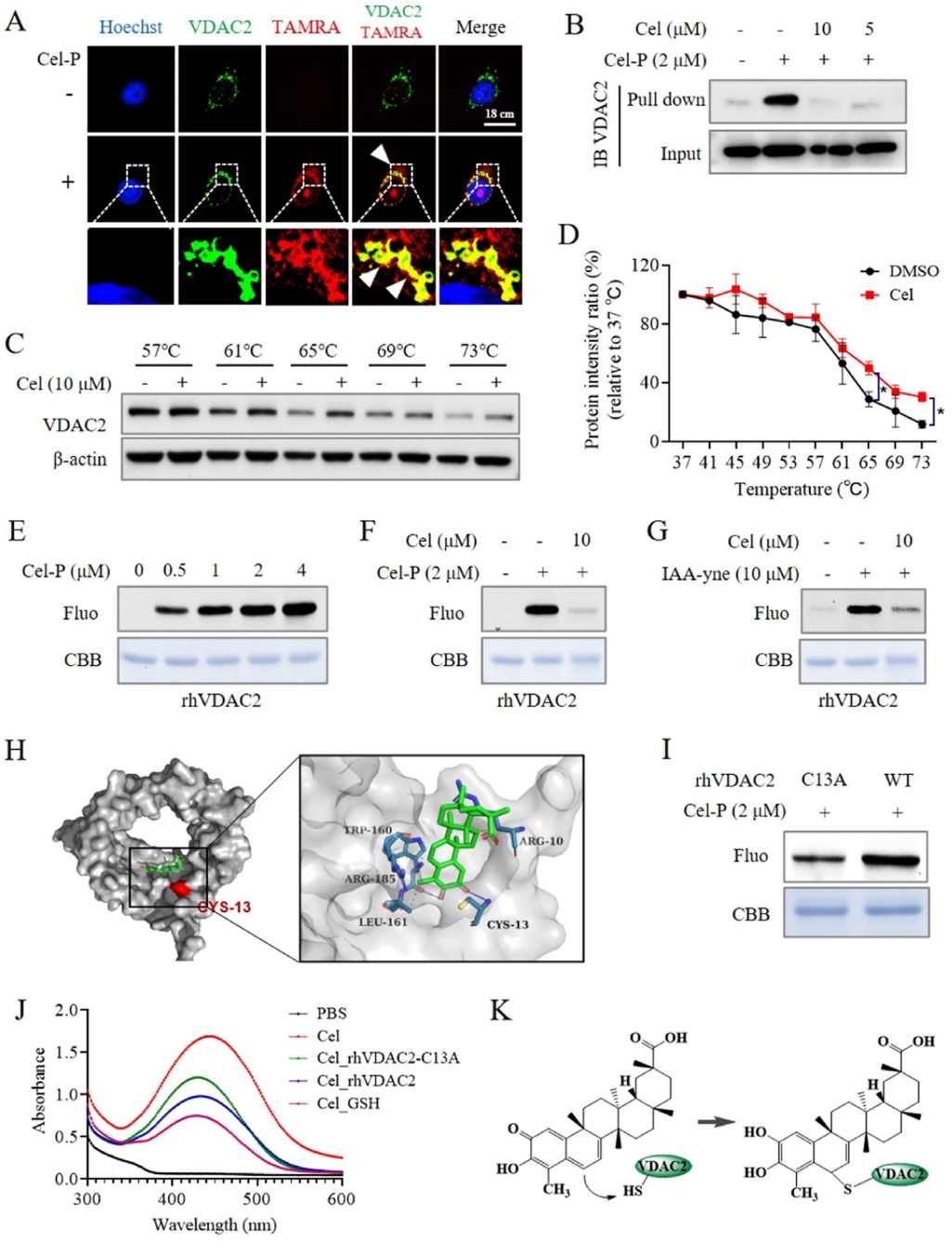

Fig. 2 – Cel directly binds to the cysteine residues of VDAC2. (A) Fluorescence staining for co-localization of VDAC2 protein (green) and Cel-P (red) (scale bar = 18 μm). (B) Protein affinity pull-down experiment by Western blotting to validate Cel directly binding to VDAC2. (C-D) CETSA-WB assay to verify the direct interaction between VDAC2 target protein and Cel. (E) Fluorescence labelling assay to demonstrate Cel targeting to rhVDAC2 protein. (F) rhVDAC2 protein incubated with Cel-P in the presence or absence of Cel, followed by fluorescence labelling assay. (G)rhVDAC2 protein incubated with IAA–yne in the presence or absence of Cel, followed by fluorescence labelling assay. (H) Molecular docking model between Cel and VDAC2 protein. (I) Fluorescence labelling assay to analyze WT rhVDAC2 and mutated Cys13 site of rhVDAC2 (C13S) proteins labelled by Cel-P. (J) UV-visible absorption spectra of Cel incubated with rhVDAC2 (WT) and rhVDAC2 (C13A). (K) Proposed mechanism of covalent modification by Cel binding to VDAC2.

protein (TSP) which is enhanced upon small molecule binding [33]. The thermal stability of VDAC2 was found to be elevated after incubation with Cel in a CETSA-WB assay, suggesting the direct interaction of Cel with VDAC2 (Fig. 2C, 2D and S2A).

We then further explored the binding mechanism of Cel to VDAC2. The electrophilic quinone methide moiety which is found in Cel is a Michael acceptor that can form a covalent adduct between small molecule drugs and the thiol of specific cysteines, and is important for the biological effect of electrophilic natural products [34,35]. At the same time, emerging studies have demonstrated that Cel can covalently bind to the thiol of cysteine residues on its target proteins to exert its biological activities [36–38]. We thus speculated whether Cel can react with the thiol of cysteine residues on VDAC2 through its electrophilic quinone methide moiety. Aiming to investigate this phenomenon, we designed an *in vitro* system with recombinant human VDAC2 (rhVDAC2) protein which was labeled with Cel-P through click chemistry using fluorescent labels for detection purposes. Expectedly, Cel-P showed evidence of a dose-dependent binding to rhVDAC2 (Fig. 2E), and the labelling could be blocked by an excessive amount of Cel (Fig. 2F). Iodoacetamide (IAA) is an essential alkylating reagent of cysteine for proteomics [39], and is the basis of the IAA–yne (IAA attached to a terminal alkyne moiety) probe commonly used for cysteine-reactivity profiling [39]. We performed similar competitive binding experiments with IAA–yne labelling of rhVDAC2 proteins followed by click reaction with fluorescence tags. We found that IAA–yne labelling of rhVDAC2 could be competed away by excess Cel (Fig. 2G), suggesting that Cel directly binds to cysteine residues of VDAC2.

To investigate the exact Cel-binding sites on the VDAC2 protein, we performed molecular dynamics docking profiling between the structures of Cel and VDAC2 protein. The molecular docking results showed the direct interaction between Cel and cysteine 13 (Cys13) of VDAC2 (Fig. 2H). Next, we conducted site-specific mutation of Cys13 of VDAC2 ($VDAC2^{C13A}$). Recombinant cysteine-mutated and wild-type (WT) VDAC2 proteins were then used for labelling experiments. The fluorescence intensity of Cel-P bound mutant $VDAC2^{C13A}$ proteins was significantly lower compared to the WT (Fig. 2I), further indicating that Cel covalently binds to Cys13 of VDAC2. Furthermore, as a complementary method to monitor the binding of Cel to the target protein [23,40], we made use of the fact that Cel shows a maximal absorption peak at approximately 425–465 nm (Fig. S2B) and that this maximal peak decreases when Cel reacts with the nucleophilic thiol [40]. As expected, our data indicated that this absorptive peak of Cel was reduced when mixed with GSH, WT rhVDAC2, while mixing with mutant $VDAC2^{C13A}$ resulted in a relatively lower reduction. (Fig. 2J and S2C-S2D). Overall, our results indicate that Cel covalently binds to the cysteine 13 residue in VDAC2 (Fig. 2K).

3.3. *Cel induces cytochrome C release via dysregulating VDAC2-mediated mPTP function*

In the outer membrane of mitochondria, there are mPTP including VDACs, adenine nucleotide translocase and Cyclophilin D [41]. Three members of the VDAC family, VDAC1, VDAC2 and VDAC3, serve a central role in regulating energy metabolism inside and outside the mitochondria, and are closely related to cell survival and death [42]. Small molecule drugs can cause abnormalities in the structure or function of VDACs, leading to disorders of mitochondrial function and result in anti-tumor effects [19,43]. Our data suggested that Cel could target to VDAC2 in the mitochondria outer membrane, leading to the release of Cyto C into the cytoplasm, causing oxidative stress and subsequently activating downstream signaling pathways. These findings will be further confirmed through subsequent experiments (Fig. 3A). The results of the fluorescence staining experiment revealed that Cel-P co-localized with mitochondria in SK-Hep1 cells, suggesting the possibility of Cel targeting to the mitochondria (Fig. 3B).

To further explore the impact of Cel on the mitochondria, we decided to measure the MMP via JC-1 staining in SK-Hep1 cells following treatment with Cel. Our results indicated that Cel caused the unbalance of MMP and disturbed the structure of mitochondrial membrane and mPTP (Fig. 3C). The disturbance of mPTP has been demonstrated to cause the release of intermembrane space proteins, such as Cyto C [44] and accelerate ROS generation [14]. We revealed that Cel induces the release of Cyto C from mitochondria into the cytoplasm by immunofluorescence staining (Fig. 3D). In addition, we further confirmed this phenomenon by using Western blotting to detect Cyto C of mitochondria or cytoplasm (Fig. 3E and 3F), and then induced the occurrence of mitochondrial apoptosis and ROS generation (Fig. 4C). It may eventually lead to cancer cell death. Collectively, our data demonstrate that Cel impedes the biological activity of VDAC2, resulting in the release of Cyto C from the mitochondria and the dysregulation of mPTP.

3.4. *Cel induces ROS-mediated ferroptosis and apoptosis via targeting VDAC2*

The VDAC family are multifunctional mitochondrial proteins participating in controlling cell ferroptosis and apoptosis [43,45]. It is interesting to note that ERA, a major ferroptosis activator, directly binds to VDAC2 and selectively induces non-apoptotic signaling pathway in hepatic cancer cells [11]. Here, we conducted further investigations into the involvement of Cel acting with VDAC2 in regulating tumor cell death and survival. We explored the global effects of Cel on protein expression at the cellular level by proteomics (Fig. 4A). Using proteomic data analysis, we identified and quantified 858 (452 up, 406 down) DEPs ($|\text{fold change}| \geq 1.5$, FDR < 0.05) after Cel treatment (Fig. 4B). Subsequently, GO enrichment of DEPs revealed Cel-regulated pathways including ferroptosis, apoptosis and ROS related signaling (Fig. 4C). We further analyzed the expressions of ferroptosis, apoptosis and ROS related proteins such as KEAP1, STEAP3, GLCM, BAD, CASP3 (Fig. 4D). Previous studies have shown that VDAC2 is involved in the regulation of mitochondria-related ferroptosis, mitochondrial ROS level and BAX-mediated apoptosis for limiting tumor development [46,47]. These could be well matched with the biological processes and functions

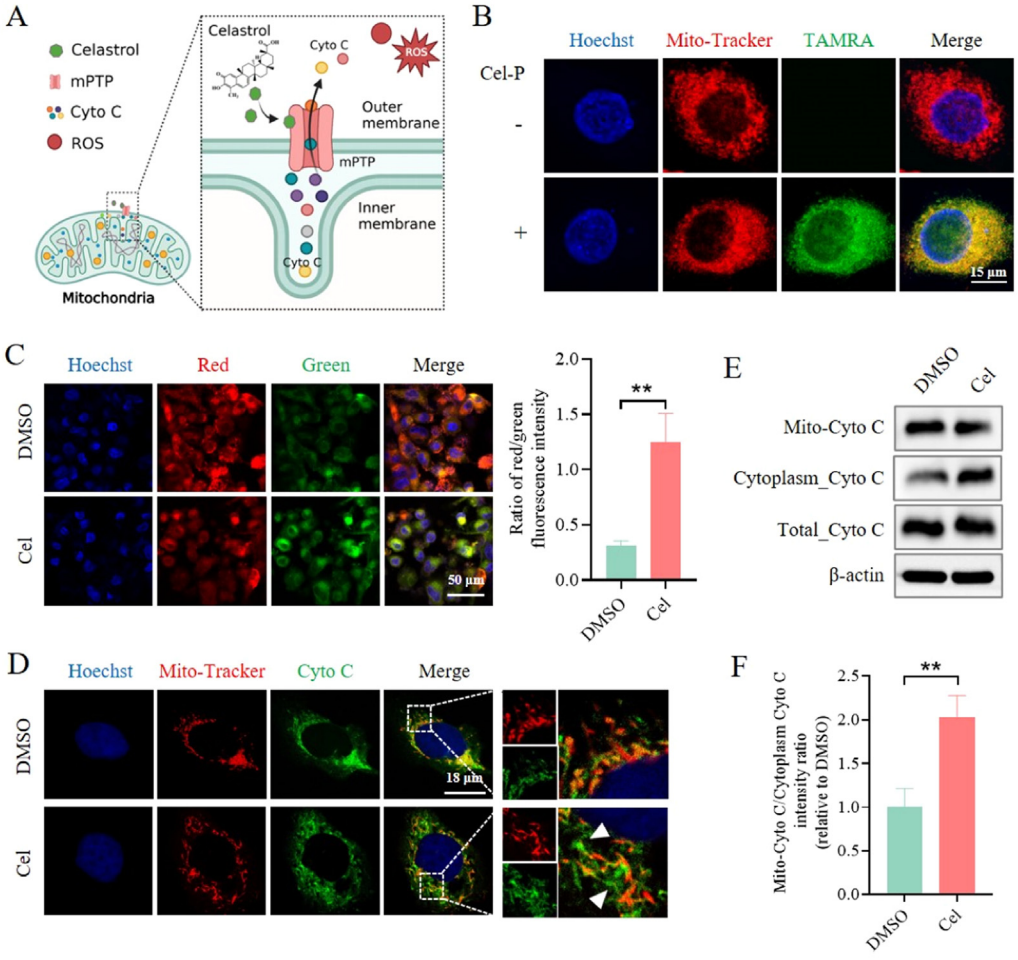

Fig. 3 – Cel interferes with the biological activity of VDAC2, leading to the dysregulation of mPTP. (A) Schematic diagram of Cel targeting mPTP or VDAC2 to induce cytochrome C release. (B) Fluorescence staining for co-localization of mito-tracker (red) and Cel-P (green) (scale bar = 15 μm). (C) Fluorescence imaging to evaluate MMP by Cel in SK-Hep1 cells (scale bar = 50 μm), mean ± SD, **P < 0.01 for Cel vs. DMSO. (D) Immunofluorescence staining to monitor the release of Cyto C by Cel in SK-Hep1 cells (scale bar = 18 μm). (E) Western blotting to detect Cyto C of mitochondria or cytoplasm by Cel in SK-Hep1 cells. (F) Corresponding densitometry analysis to Figure E, mean ± SD, **P < 0.01 for Cel vs. DMSO.

of VDAC2, suggesting that Cel binding to VDAC2 induces ferroptosis and apoptosis in hepatic cancer cells.

We previously showed that Cel has the potential to trigger ferroptotic cell death in activated hepatic stellate cells, thus alleviating liver fibrosis [23]. To elucidate clearly the involvement of ferroptosis in the anti-tumor effect of Cel, we examined the levels of several markers of ferroptosis including ROS, GSH, iron ions (Fe^{2+}/Fe^{3+}), and LPO at the cellular level. DFO (a ferroptotic inhibitor), ERA (a ferroptotic activitor) and NAC (a lipophilic antioxidant) were used in the next examined experiments. Firstly, ROS generation significantly increased in hepatic cancer cells after Cel treatment, while NAC could effectively weaken this effect (Fig. 4E). Cel induced the generation of ROS in hepatic cancer cells as observed by electron microscopy. Pretreatment of cells with NAC significantly reduced the generation of ROS (Fig. S3A). In addition, according to our findings, treating hepatic cancer cells with Cel resulted in cytotoxicity. However, this effect was reversed by the administration of both DFO and NAC. Interestingly, ERA had the opposite effect and enhanced the cytotoxicity of Cel in these cells (Fig. 4F). Moreover, Cel remarkably decreased GSH levels and enhanced the levels of Fe^{2+}/$Fe^{3+}$and LPO, while co-incubation with ERA could synergistically enhance these effects of Cel. On the other hand, co-incubation with DFO and NAC could significantly elevate GSH levels and decrease the levels of Fe^{2+}/$Fe^{3+}$and LPO (Fig. 4G-4H and S3B-S3E).

Some studies have revealed that Cel could induce mitochondrial dysfucntion to lead to apoptotic cell death in tumor cells [48,49]. For instance, Cel was found to elevate cellular ROS levels and ROS-mediated mitochondrial apoptosis in cancer cells [16]. Moreover, targeting ferroptosis and apoptosis is considered a novel strategy for the treatment of tumors by triggering ROS-related signaling pathway [50]. In parallel, we also examined the expression of proteins pro-apoptotic Bad and cleaved Caspase-3 involved in mediating mitochondrial apoptosis. Results indicated that Cel elevated the ratio of Bax/Bcl-2 expression, and facilitated Cyto C

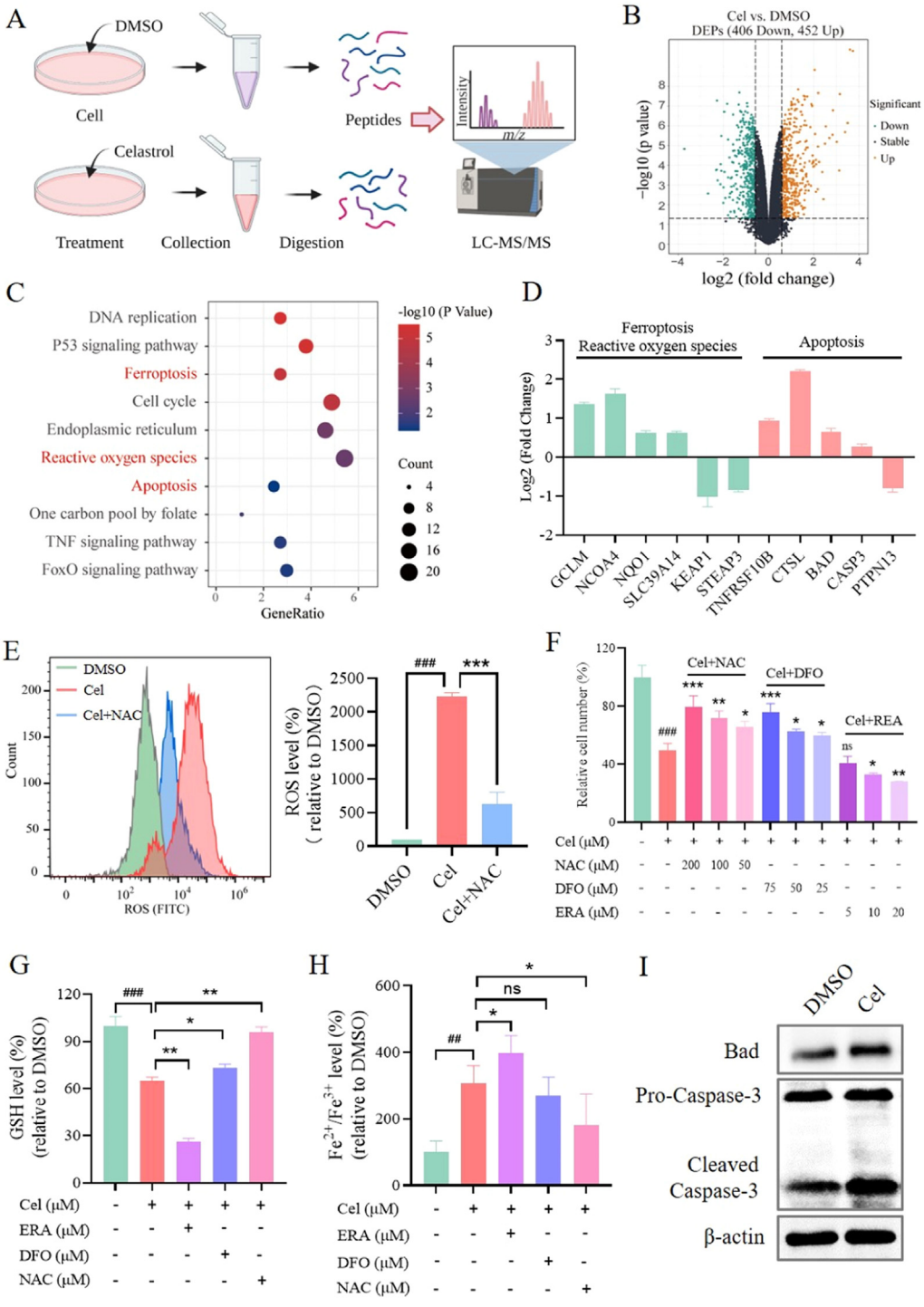

Fig. 4 – Cel triggers ROS-mediated ferroptosis and apoptosis via targeting VDAC2. (A) The workflow of proteomic analysis for Cel-treated hepatic cancer cells. (B) Volcano plot indicating differentially expressed proteins (DEPs) (orange, up; stable, black; green, down) in Cel treatment vs DMSO groups. (C) Gene ontology (GO) enrichment of DEPs in regulating pathways in hepatic cancer cells after Cel treatment. (D) DEPs of ferroptosis, apoptosis and ROS-related proteins in Cel treatment vs DMSO groups. (E) Flow cytometry to measure ROS levels in different groups (Cel or co-incubated with NAC) in hepatic cancer cells (mean ± SD, $n = 3$; $^{###}P < 0.001$ vs. DMSO; $^{***}P < 0.001$ vs. Cel). (F) The impact of DFO, ERA, and NAC on Cel-treated cell viability (mean ± SD, $n = 3$; $^{*}P < 0.05$, $^{**}P < 0.01$, $^{***}P < 0.001$ vs. Cel; $^{###}P < 0.001$ vs. DMSO; ns, no significance). (G-H) Effects of ERA, DFO or NAC on Cel-induced ferroptotic markers (GSH and Fe^{2+}/Fe^{3+} LPO levels) in hepatic cancer cells (mean ± SD, $n = 3$; $^{*}P < 0.05$, $^{**}P < 0.01$ vs. Cel; $^{##}P < 0.01$, $^{###}P < 0.001$ vs. DMSO; ns, no significance). (I) Examination of the pro-apoptotic Bad and cleaved Caspase-3 expression by Cel in hepatic cancer cells.

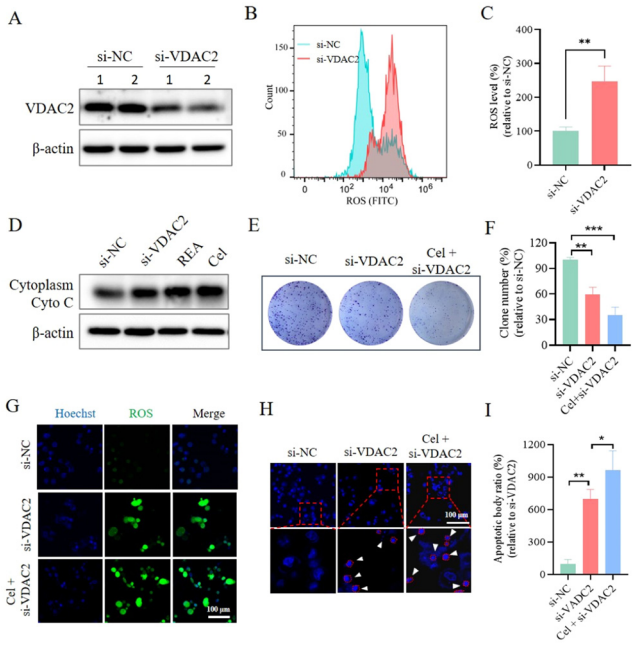

Fig. 5 – Knockdown of VDAC2 aggravates Cel-induced mitochondrial dependent cell death. (A) Western blotting analysis to evaluate the knockdown efficiency of VDAC2 in hepatic cancer cells. (B-C) Flow cytometry to monitor the ROS levels of WT and VDAC2^{KD} cells, (mean ± SD, $n = 3$; $^{**}P < 0.01$ vs. si-NC). (D) Western blotting analysis to measure the release of Cyto C into cytoplasm in WT and VDAC2^{KD} cells. (E-F) Colony formation assay was used to assess the proliferation of WT and VDAC2 ^{KD} cells, (mean ± SD, $n = 3$; $^{**}P < 0.01$, $^{***}P < 0.001$, vs. si-NC). (G) Fluorescence imaging to detect the ROS levels of WT and VDAC2^{KD} cells (scale bar = 100 μm). (H) Detection of apoptotic bodies by Cel in VDAC2^{KD} cells (scale bar = 100 μm). (mean ± SD, $n = 3$; $^{*}P < 0.05$, $^{**}P < 0.01$, vs. si-NC).

to activate the caspase-3-mediated mitochondrial apoptotic pathway (Fig. 4I). We also found that Cel induces the generation of apoptotic bodies in hepatic cancer cells (Fig. S3F-S3G). Taken together, these results confirmed that Cel has potential anti-tumor properties that are attributed to the triggering of ROS-mediated apoptosis and ferroptosis mechanisms in hepatic cancer cells.

3.5. *Knockdown of VDAC2 aggravates Cel-induced mitochondrial dependent cell death*

To functionally verify that VDAC2 is an important target protein in the regulation of ferroptosis and apoptosis to exhibit its anti-tumor activity, we employed small siRNA (Table S1) to knockdown VDAC2 (VDAC2^{KD}) in hepatic cancer cells. VDAC2 was effectively knocked down as assayed by Western blotting analysis (Fig. 5A). Upon knockdown of VDAC2, Cyto C was released from mitochondria into the cytoplasm in VDAC2^{KD} cells by Western blotting (Fig. 5D), resulting in the elevation of ROS levels (Fig. 5B and 5C). As reported in previous studies, Cyto C from mitochondria into the cytoplasm leads to ROS production [51].

However, VDAC2 knockdown significantly restrained the viability and proliferation of hepatic cancer cells (Fig. 5E-5F). On one hand, VDAC2 knockdown aggravated ROS generation by Cel in VDAC2^{KD} cells (Fig. 5G and S3H). On the other hand, this knockdown of VDAC2 remarkably induced the generation of apoptotic bodies by Cel in VDAC2^{KD} cells (Fig. 5G-5I). Similar to the current work, loss of VDAC2 has been reported to result in PCD in cancer cells [19]. In summary, these data show that the knockdown of VDAC2 induces ROS-mediated cell death in hepatic cancer cells, Cel could further aggravate cellular apoptosis in VDAC2^{KD} cells.

3.6. *Cel liposomes were designed to improve anti-tumor targetability*

Cel is a natural triterpenoid compound derived from Tripterygium wilfordii herb [15]. It has been reported to exhibit multiple biological activities, including suppressing the proliferation and growth of liver cancer, gastric carcinoma [16,52]. Here, our data showed that Cel could induce ferroptosis and apoptosis by targeting VDAC2 protein, thereby exerting its anti-liver cancer activity. Thus, Cel may be a candidate compound for the management of liver cancer. However, the severe side effects caused by Cel represent a major barrier to any possible clinical application [53]. To address these problems, we developed alkyl N-octyl-β-D-glucopyranoside-modified Cel liposomes (Alkyl-Glu-Cel-LS, AGCL), based on the idea that coencapsulation of Cel into alkyl glucoside (Alkyl-Glu)-modified liposomes could improve its tumor targetability and minimize its side effects. We used a solvent displacement method to effectively load Cel into GLUT1-targeting AGCL in order to construct AGCL (Fig. 6A).

In our previous study, we have exploited alkyl glucoside-modified artemisinin liposomes to enhance its anti-liver tumor activity [22]. The appearance of Alkyl-Glu-modified liposomes (Alkyl-Glu-LS, AGL) and AGCL are shown in Fig. 6B. TEM result indicated that the morphology of AGCL was regular spherical (Fig. S4A). FTIR spectrum of AGCL (Fig. S4B) indicated that the peaks for C=O strechning vibration at 1735.70 cm^{-1}, PO_2 symmetric stretching vibration at 1084.79 cm^{-1} and PO_2 assymetric stretching vibration at 1231.67 cm^{-1}, which were characteristic bands of phospholipid [54,55]. The C–O stretching vibration of DSPE-mPEG2000 and N-octyl-β-D-glucopyranoside had influence on the C–O stretching vibration of AGCL. The characteristic peaks of Cel and cholesterol in AGCL were not obvious in the fingerprint region of FTIR spectrum (1300–400 cm^{-1}) (Fig. S4B), this indicated the Cel and cholesterol had been loaded in AGCL [56]. In addition, AGCL, Cel and other materials were analysed for XRD (Fig. S4E). The characteristic peaks of Cel at 10.81°, 16.89° and 19.46°, the characteristic peaks of cholesterol at 16.32°, 17.76° and 19.54°, and the characteristic peaks of N-octyl-β-D-glucopyranoside at 13.46°, 22.46° and 36.96° were absent in the XRD spectrum of AGCL. This indicated that Cel, cholesterol and N-octyl-β-D-glucopyranoside were as amorphous form in AGCL [56,57]. Zeta potential, PDI and particle size of the AGCL were confirmed by using a nanoparticle sizer to be approximately 83.41±0.39 nm,

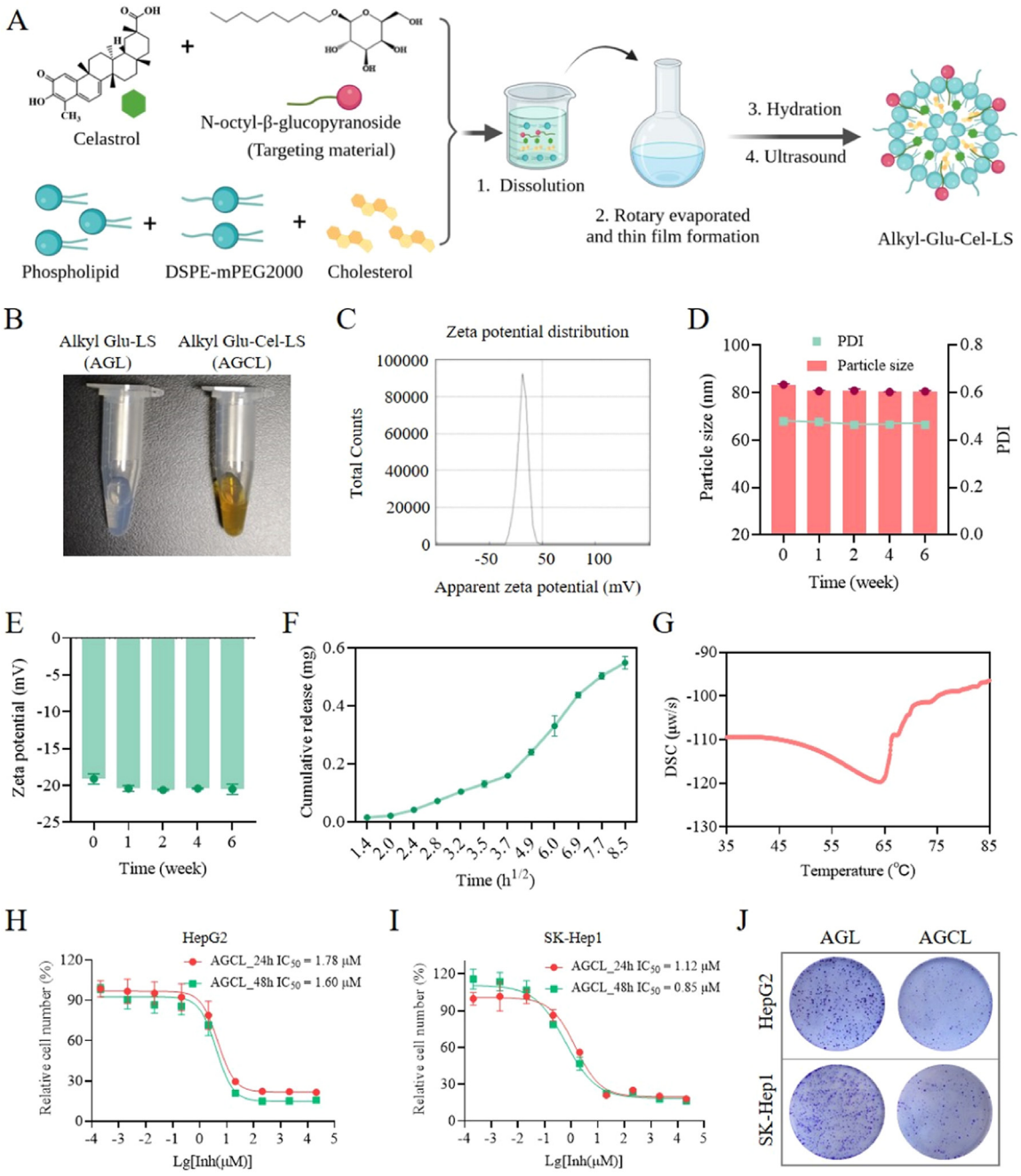

Fig. 6 – Cel liposomes were designed to improve anti-tumor targetability. (A) The workflow of Alkyl-Glu-modified Cel liposomes. (B) Appearances of AGL and AGCL. (C) The zeta potential of AGCL ($n = 3$). (D) Particle size and PDI of AGCL over a period of 42 d ($n = 3$). (E) The zeta potential of AGCL over a period of 42 d ($n = 3$). (F) The drug release of AGCL ($n = 3$). (G) DSC of AGCL was measured by a Nano Differential Scanning Calorimeter ($n = 3$). (H-I) Inhibition of SK-hep1 and Hepg2 cell lines proliferation by AGCL was evaluated by CCK-8 assay for 24 h or 48 h ($n = 3$). (J) Colony formation assay is used to assess proliferative activity of AGCL in SK-hep1 and Hepg2 cells.

0.480±0.005 and −19.1 ± 0.7 mV (Fig. 6C), respectively. Furthermore, the drug release characteristics of AGCL was consistent with the law of Higuchi kinetics equation, and the drug release rate of AGCL was 0.0816 mg·h$^{1/2}$ (Fig. 6F). The phase transition temperature of AGCL was determined by using a Nano Differential Scanning Calorimeter, with results showing that the main phase-transition temperature of AGCL was 64.21 °C (Fig. 6G). The appearance of AGCL remained a red semitransparent liquid during the 6-week storage period at 4 °C. The Characterizations of liposomes were tested at different sampling points (Fig. 6D-6F). RSDs of particle size, PDI and zeta potential of AGCL were 1.57 %, 1.60 % and 3.07 %, respectively. The above data indicated that AGCL could be stably stored at 4 °C for at least 6 weeks.

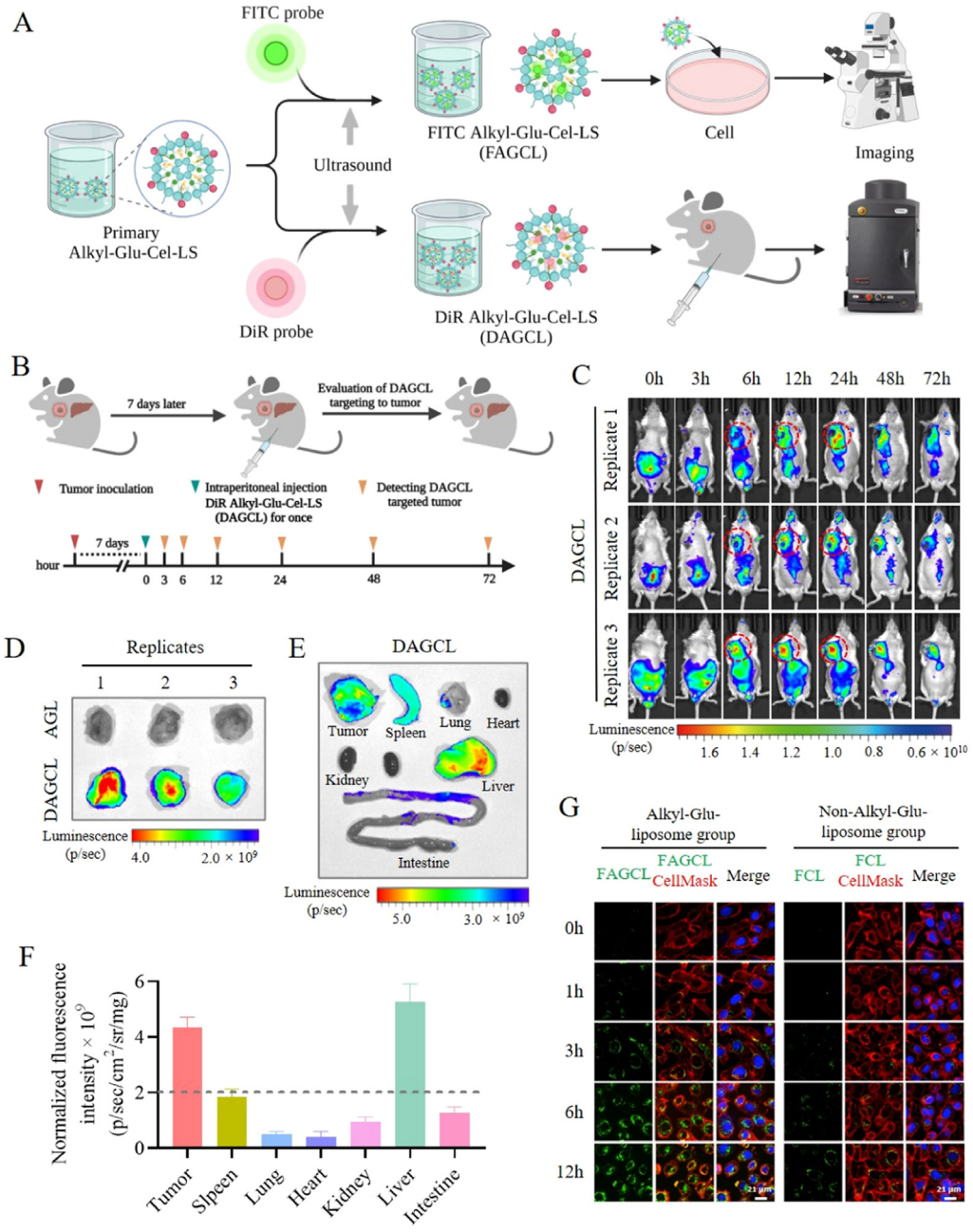

Fig. 7 – Cellular uptake efficacy and biodistribution of Cel liposomes are evaluated *in vitro* and *in vivo*. (A) The synthetic workflow of FITC Alkyl-Glu-Cel-LS and DiR Alkyl-Glu-Cel-LS liposomes. (B) Experimental scheme of preparation of ectopic liver cancer models and biodistribution of DAGCL *in vivo*. (C) *In vivo* targeting imaging of liver cancer models in mice at 0, 3, 6, 12, 24, 48 and 72 h after intraperitoneal (i.p.) injection of DAGCL solution. (D) Representative images of tumors 24 h after administration of AGL or DAGCL solution. (E) Representative images of different tissues and tumors 24 h after treatment of DAGCL solution. (F) Quantification of DAGCL accumulation in different tissues and tumors. (G) Cellular uptake efficacy of Cel-nanomedicine by microscopy imaging (scale bar = 60 μm).

We next evaluated the cytotoxicity of AGCL in SK-Hep1 and HepG2 cells. AGCL remarkably suppressed the proliferative activity of SK-Hep1 and HepG2 cells by cytotoxic assay after treatment for 24 or 48 h (Fig. 6H and 6I). AGCL was found to inhibit the proliferation of SK-Hep1 and HepG2 cells as seen in the colony formation assay (Fig. 6J), indicating that AGCL had effective cytotoxicity in liver cancer cells.

3.7. *Cellular uptake efficacy and biodistribution of Cel liposomes are evaluated* in vitro *and* in vivo

GLUT1 mediates the transmembrane transport of glucose in tumor cells [58,59]. It has been reported that GLUT1 is a key regulator of glucose metabolism [60], controlling the energy intake of cancer cells [61]. Importantly, GLUT1-targeting AGCL

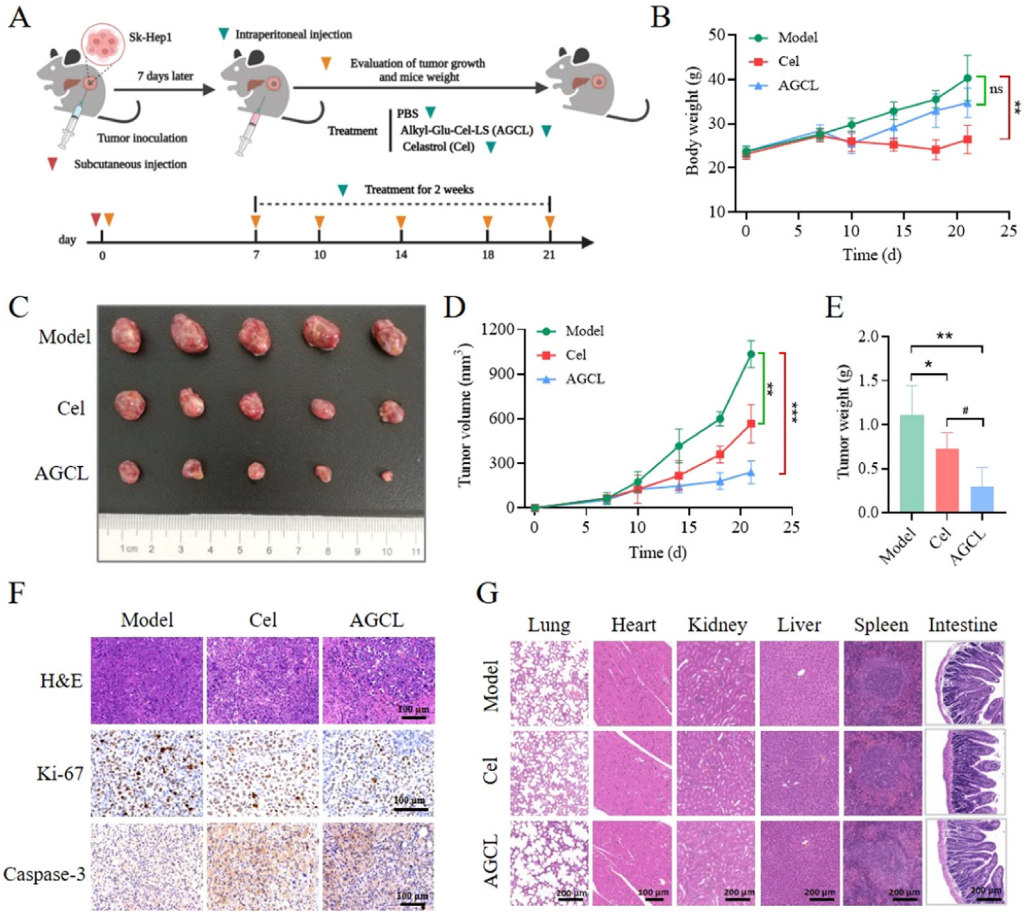

Fig. 8 – Cel liposomes could effectively inhibit the growth of xenograft tumor. There are three groups: Model group, a saline-treated xenograft model mice group; Cel group, a Cel-treated xenograft model mice group; AGCL group, an AGCL-treated xenograft model mice group. (A) Experimental scheme to examine the inhibitory effect of AGCL on xenograft models. (B) Body weight curves of xenograft model mice in three groups (mean ± SD, $n = 5$, $^{**}P < 0.01$ vs. Model; ns, no significance). (C) Representative morphology of tumor in three groups after treatment for 14 d (D) Tumor volumes were measured after AGCL or Cel treatment, (mean ± SD, $n = 5$, $^{**}P < 0.01$, $^{***}P < 0.001$ vs. Model). (E) Statistics analysis of tumor weights (mean ± SD, $n = 5$, $^{*}P < 0.05$, $^{**}P < 0.01$ vs. Model). (F) H&E staining to examine the effect of AGCL or Cel on tumor tissues. Anti-proliferation and apoptotic protein (Ki-57 and Caspase-3) effects be detected by immunohistochemistry staining (scale bar = 100 μm). (G) H&E staining to examine the effect of AGCL or Cel on major organs including lung, kidney, liver, spleen and intestine (scale bar = 200 μm) and heart (scale bar = 100 μm).

can accumulate in tumor tissues much more compared to other normal organs [22]. To assess the cellular uptake and systemic distribution of AGCL, we further designed and prepared DAGCL (Fig. 7A). Subsequently, to evaluate the cellular uptake efficiency of DAGCL (DAGCL equivalent to 1 mg/kg Cel) in tumor cells, H22 tumor-bearing mice were prepared to investigate the tumor targetability and biodistribution of DAGCL (Fig. 7B). Firstly, *in vivo* fluorescence imaging assay was carried out in xenograft mice at 0, 3, 6, 12, 24, 48 and 72 h after intraperitoneal (i.p.) injection of DAGCL solution. In the initial stage, the fluorescence signal was mainly concentrated in the mouse abdomens. Movement of DAGCL from the abdomen to the tumor tissue could be clearly observed from 6 to 24 h after injection. Following administration for 48 h, the fluorescent signal diminished gradually (Fig. 7C). To further determine the tumor targeting of DAGCL, we dissected different tissues (tumor, spleen, lung, heart, kidney, liver and intestine) from mice 24 h after administration for fluorescence intensity detection. As expected, DAGCL was mainly accumulated in the tumor and liver after administration 24 h later, while DAGCL exhibited prolonged circulation with notably time-dependent targeting tumor during the period from 0 to 24 h after injection (Fig. 7D-7F and S4F).

Moreover, we also performed *in vitro* uptake assays in HepG2 cells by fluorescence imaging. FITC fluorescent-labeled liposomes (FITC Alkyl-Glu-Cel-LS, FAGCL or FITC Cel-LS, FCL) were designed and prepared. HepG2 cells were incubated with FAGCL or FCL, and then FAGCL or FCL uptake by cells was detected at 0, 1,3, 6,12 h, respectively. As anticipated, FAGCL displayed an uptake increase that was time-dependent in HepG2, and absorbed into cell membrane

faster by cancer cells than liposomes without Alkyl-Glu (FCL) (Fig. 7G). Thus, *in vitro* uptake experiments have shown that Alkyl-Glu-could enhance the absorption of liposomes by cancer cells. Moreover, the fluorescent liposomes exhibited comparable efficacy to AGCL in inhibiting the proliferation of hepatic cancer cells (Fig. S4C-S4D). Overall, these findings demonstrate that AGCL has good biological targeting and uptake by cell *in vitro* and *in vivo*.

3.8. *Cel liposomes could effectively inhibit the growth of xenograft tumor*

To examine the effect of AGCL and Cel on the tumor inhibition *in vivo*, we established a xenograft model by subcutaneously injecting cells into the flank of nude mice [62]. On the one hand, xenograft mice were administered with AGCL (the liposomes equivalent to 1 mg/kg Cel) or Cel (1 mg/kg) by intraperitoneal injection (i.p.), once daily for 5 d each week when the tumors grew up to around 50 mm^3. On the other hand, xenograft mice received the saline vehicle as model group (Fig. 8A). The experimental findings demonstrated that both AGCL and Cel significantly inhibited tumor progression in the xenograft models by reducing the tumor size and weight. (Fig. 8C–8E). Cel has shown potential in inhibiting tumors, but AGCL exhibited a more potent tumor-inhibiting effect. Consequently, AGCL's therapeutic effect is significantly superior to that of Cel. At the same time, histological analysis of tumors revealed that AGCL and Cel induced tumor necroptosis and decreased tumor cell Ki-67 immunoreactivity (Fig. 8F). Finally, we assessed the comparative toxicities of Cel and AGCL in mice by monitoring body weight, organ physiology and serum indicators. Neither treatment resulted in observable pathological changes in mouse lungs, hearts, kidneys, livers and spleens as assessed by H&E staining (Fig. 8G), nor significant changes in serum biochemical indicators (Fig. S5). However, Cel treatment significantly reduced mouse body weight, while AGCL had no significant effect (Fig. 8B). There was a phenomenon that mice had loose stool or diarrhea, while AGCL did not have this phenomenon. The main reason for this phenomenon should be that Cel has certain damage to intestinal villi, while AGCL has almost no damage (Fig. 8G). In addition, both AGCL and Cel treatment up-regulated the expression of Caspase-3, but the effect of AGCL was better than that of Cel. In summary, AGCL plays a role in slow release, enhances anti-tumor effect and alleviates the stimulating effect on the intestine to reduce toxicity.

4. Conclusions

In summary, the present study demonstrated that Cel could directly bind to VDAC2 to induce mitochondria-dependent cell death in liver cancer cells. Further study indicated that targeting cysteine residues of VDAC2 by Cel results in the release of Cyto C into the cytosol, inducing ROS-mediated mitochondrial apoptosis or ferroptosis in liver cancer cells. Additionally, by co-encapsulating Cel within Alkyl-Glu-modified liposomes at a low dosage, the anti-tumor efficacy of Cel was improved while reducing its potential side effects. AGCL mediated targeting delivery of Cel, inhibited the proliferation and growth of tumor and triggered apoptotic cell death, demonstrating an effective anti-HCC effect. The low dosage requirement of Cel liposomes will provide great benefits to patients suffering from HCC due to its high efficacy with minimal side effects. Our study validates the potential role of VDAC2 as a direct effector causing Cel-mediated cell death in cancer cells, and further highlights the augmented effectiveness and decreased toxicity of Cel when co-encapsulated within liposomes.

Conflicts of interest

The authors declare no conflicts of interest. The authors alone are responsible for the content and writing of this article.

Acknowledgments

This study received financial support from the National Natural Science Foundation of China (Grants No. 82304827, 82074098, and 81841001), the Fundamental Research Funds for the Central public welfare research institutes (ZZ13-ZD-07), the National Key Research and Development Program of China (2020YFA0908000 and 2022YFC2303600), the Innovation Team and Talents Cultivation Program of National Administration of Traditional Chinese Medicine (No: ZYYCXTD-C-202002), The Shenzhen Medical Research Fund of Shenzhen Medical Academy of Research and Translation (B2302051), the Fundamental Research Funds for the Central Public Welfare Research Institutes (Grants No. ZZ13-YQ-108), the Shenzhen Science and Technology Innovation Commission (Grants No. JCYJ20210324115800001, the Science and Technology Foundation of Shenzhen (Shenzhen Clinical Medical Research Center for Geriatric Diseases), the Distinguished Expert Project of Sichuan Province Tianfu Scholar (CW202002), Supported by Shenzhen Governmental Sustainable Development Fund (KCXFZ20201221173612034); Supported by Shenzhen key Laboratory of Kidney Diseases (ZDSYS201504301616234); Supported by Shenzhen Fund for Guangdong Provincial High-level Clinical Key Specialties (NO.SZGSP001).

Supplementary materials

Supplementary material associated with this article can be found, in the online version, at doi:10.1016/j.ajps.2023.100874.

References

[1] Dixon SJ, Lemberg KM, Lamprecht MR, Skouta R, Zaitsev EM, Gleason CE, et al. Ferroptosis: an iron-dependent form of nonapoptotic cell death. Cell 2012;149:1060–72.
[2] Baechler BL, Bloemberg D, Quadrilatero J. Mitophagy regulates mitochondrial network signaling, oxidative stress, and apoptosis during myoblast differentiation. Autophagy 2019;15:1606–19.
[3] Yang Y, Luo M, Zhang K. Nedd4 ubiquitylates VDAC2/3 to suppress erastin-induced ferroptosis in melanoma. Nat Commun 2020;11:433.

[4] Wei R, Cao J, Yao S. Matrine promotes liver cancer cell apoptosis by inhibiting mitophagy and PINK1/Parkin pathways. Cell Stress Chaperones 2018;23:1295–1309.
[5] Rademaker G, Boumahd Y, Peiffer R, Anania S, Wissocq T, Liégeois M, et al. Myoferlin targeting triggers mitophagy and primes ferroptosis in pancreatic cancer cells. Redox Biol 2022;53:102324.
[6] Yang M, Wu X, Hu J, Wang Y, Wang Y, Zhang L, et al. COMMD10 inhibits HIF1α/CP loop to enhance ferroptosis and radiosensitivity by disrupting Cu-Fe balance in hepatocellular carcinoma. J Hepatol 2022;76:1138–50.
[7] Lei Y, Gan H, Huang Y, Chen Y, Chen L, Shan A, et al. Digitoxin inhibits proliferation of multidrug-resistant HepG2 cells through G(2)/M cell cycle arrest and apoptosis. Oncol Lett 2020;20:71.
[8] Yang Y, Zuo S, Li L, Kuang X, Li J, Sun B, et al. Iron-doxorubicin prodrug loaded liposome nanogenerator programs multimodal ferroptosis for efficient cancer therapy. Asian J Pharm Sci 2021;16:784–93.
[9] Baker MA, Lane DJ, Ly JD, De Pinto V, Lawen A. VDAC1 is a transplasma membrane NADH-ferricyanide reductase. J Biol Chem 2004;279:4811–19.
[10] Mazure NM. VDAC in cancer. Biochimica et Biophysica Acta Bioenergetics 2017;1858:665–73.
[11] Yagoda N, von Rechenberg M, Zaganjor E, Bauer AJ, Yang WS, Fridman DJ, et al. RAS-RAF-MEK-dependent oxidative cell death involving voltage-dependent anion channels. Nature 2007;447:864–8.
[12] Zhao Y, Li Y, Zhang R, Wang F, Wang T. The role of erastin in ferroptosis and its prospects in cancer therapy. Onco Targets Ther 2020;13:5429–41.
[13] Scharstuhl A, Mutsaers HA, Pennings SW, Russel FG, Wagener FA. Involvement of VDAC, Bax and ceramides in the efflux of AIF from mitochondria during curcumin-induced apoptosis. PLoS ONE 2009;4:e6688.
[14] DeHart DN, Fang D, Heslop K, Li L, Lemasters JJ, Maldonado EN. Opening of voltage dependent anion channels promotes reactive oxygen species generation, mitochondrial dysfunction and cell death in cancer cells. Biochem Pharmacol 2018;148:155–62.
[15] Kannaiyan R, Shanmugam MK, Sethi G. Molecular targets of celastrol derived from Thunder of God Vine: potential role in the treatment of inflammatory disorders and cancer. Cancer Lett 2011;303:9–20.
[16] Chen X, Zhao Y, Luo W, Chen S, Lin F, Zhang X, et al. Celastrol induces ROS-mediated apoptosis via directly targeting peroxiredoxin-2 in gastric cancer cells. Theranostics 2020;10:10290–308.
[17] Xu H, Zhao H, Ding C. Celastrol suppresses colorectal cancer via covalent targeting peroxiredoxin 1. Signal Transduct Targeted Therapy 2023;8:51.
[18] Corson TW, Crews CM. Molecular understanding and modern application of traditional medicines: triumphs and trials. Cell 2007;130:769–74.
[19] Dadsena S, Bockelmann S, Mina JGM. Ceramides bind VDAC2 to trigger mitochondrial apoptosis. Nat Commun 2019;10:1832.
[20] Qiao C, Wang H, Guan Q, Wei M, Li Z. Ferroptosis-based nano delivery systems targeted therapy for colorectal cancer: insights and future perspectives. Asian J Pharm Sci 2022;17:613–29.
[21] Zhang Z, Ji Y, Hu N, Yu Q, Zhang X, Li J, et al. Ferroptosis-induced anticancer effect of resveratrol with a biomimetic nano-delivery system in colorectal cancer treatment. Asian J Pharm Sci 2022;17:751–66.
[22] Shen S, Du M, Liu Q, Gao P, Wang J, Liu S, et al. Development of GLUT1-targeting alkyl glucoside-modified dihydroartemisinin liposomes for cancer therapy. Nanoscale 2020;12:21901–12.
[23] Luo P, Liu D, Zhang Q, Yang F, Wong YK, Xia F, et al. Celastrol induces ferroptosis in activated HSCs to ameliorate hepatic fibrosis via targeting peroxiredoxins and HO-1. Acta Pharmaceutica Sinica B 2022;12:2300–14.
[24] Zhang Q, Luo P, Xia F, Tang H, Chen J, Zhang J, et al. Capsaicin ameliorates inflammation in a TRPV1-independent mechanism by inhibiting PKM2-LDHA-mediated Warburg effect in sepsis. Cell Chem Biol 2022;29 1248-59.e6.
[25] Gu L, Zhang J, Liu D, Chen J, Liu S, Peng Q, et al. Development of artesunate intelligent prodrug liposomes based on mitochondrial targeting strategy. J Nanobiotechnol 2022;20:376.
[26] Zhao W, Zhang L, Xu Y, Zhang Z, Ren G, Tang K, et al. Hepatic stellate cells promote tumor progression by enhancement of immunosuppressive cells in an orthotopic liver tumor mouse model. Lab Invest 2014;94:182–91.
[27] Li M, Xie F, Wang L, Zhu G, Qi LW, Jiang S. Celastrol: an update on its hepatoprotective properties and the linked molecular mechanisms. Front Pharmacol 2022;13:857956.
[28] Du S, Song X, Li Y, Cao Y, Chu F, Durojaye OA, et al. Celastrol inhibits ezrin-mediated migration of hepatocellular carcinoma cells. Sci Rep 2020;10:11273.
[29] Wright MH, Sieber SA. Chemical proteomics approaches for identifying the cellular targets of natural products. Nat Prod Rep 2016;33:681–708.
[30] Wang J, Zhang CJ, Chia WN, Loh CC, Li Z, Lee YM. Haem-activated promiscuous targeting of artemisinin in Plasmodium falciparum. Nat Commun 2015;6:10111.
[31] Liu DD, Luo P, Gu L, Zhang Q, Gao P, Zhu Y, et al. Celastrol exerts a neuroprotective effect by directly binding to HMGB1 protein in cerebral ischemia-reperfusion. J Neuroinflammation 2021;18:174.
[32] Wang Z, Qin J, Zhao J, Li J, Li D, Popp M, et al. Inflammatory IFIT3 renders chemotherapy resistance by regulating post-translational modification of VDAC2 in pancreatic cancer. Theranostics 2020;10:7178–92.
[33] Martinez Molina D, Jafari R, Ignatushchenko M, Seki T, Larsson EA, Dan C, et al. Monitoring drug target engagement in cells and tissues using the cellular thermal shift assay. Science 2013;341:84–7.
[34] Gersch M, Kreuzer J, Sieber SA. Electrophilic natural products and their biological targets. Nat Prod Rep 2012;29:659–82.
[35] Maurais AJ, Weerapana E. Reactive-cysteine profiling for drug discovery. Curr Opin Chem Biol 2019;50:29–36.
[36] Sreeramulu S, Gande SL, Göbel M, Schwalbe H. Molecular mechanism of inhibition of the human protein complex Hsp90-Cdc37, a kinome chaperone-cochaperone, by triterpene celastrol. Angew Chem Int Ed Engl 2009;48:5853–5.
[37] Luo D, Fan N, Zhang X, Ngo FY, Zhao J, Zhao W, et al. Covalent inhibition of endoplasmic reticulum chaperone GRP78 disconnects the transduction of ER stress signals to inflammation and lipid accumulation in diet-induced obese mice. eLife 2022:11.
[38] Fan N, Zhang X, Zhao W, Zhao J, Luo D, Sun Y, et al. Covalent inhibition of pyruvate kinase M2 reprograms metabolic and inflammatory pathways in hepatic macrophages against non-alcoholic fatty liver disease. Int J Biol Sci 2022;18:5260–75.
[39] Abo M, Li C, Weerapana E. Isotopically-labeled iodoacetamide-alkyne probes for quantitative cysteine-reactivity profiling. Mol Pharm 2018;15:743–9.
[40] Zhang D, Chen Z, Hu C, Yan S, Li Z, Lian B, et al. Celastrol binds to its target protein via specific noncovalent interactions and reversible covalent bonds. Chem Commun (Camb) 2018;54:12871–4.
[41] Krasnov GS, Dmitriev AA, Lakunina VA, Kirpiy AA, Kudryavtseva AV. Targeting VDAC-bound hexokinase II:

a promising approach for concomitant anti-cancer therapy. Expert Opin Ther Targets 2013;17:1221–33.
[42] Shoshan-Barmatz V, Israelson A, Brdiczka D, Sheu SS. The voltage-dependent anion channel (VDAC): function in intracellular signalling, cell life and cell death. Curr Pharm Des 2006;12:2249–70.
[43] Shoshan-Barmatz V, De Pinto V, Zweckstetter M, Raviv Z, Keinan N, Arbel N. VDAC, a multi-functional mitochondrial protein regulating cell life and death. Mol Aspects Med 2010;31:227–85.
[44] Tait SW, Green DR. Mitochondrial regulation of cell death. Cold Spring Harb Perspect Biol 2013;5.
[45] Naghdi S, Várnai P, Hajnóczky G. Motifs of VDAC2 required for mitochondrial Bak import and tBid-induced apoptosis. Proc Natl Acad Sci USA 2015;112:E5590–9.
[46] Chin HS, Li MX, Tan IKL, Ninnis RL, Reljic B, Scicluna K, et al. VDAC2 enables BAX to mediate apoptosis and limit tumor development. Nat Commun 2018;9:4976.
[47] She H, Tan L, Du Y, Zhou Y, Guo N, Zhang J, et al. VDAC2 malonylation participates in sepsis-induced myocardial dysfunction via mitochondrial-related ferroptosis. Int J Biol Sci 2023;19:3143–58.
[48] Li PP, He W, Yuan PF, Song SS, Lu JT, Wei W. Celastrol induces mitochondria-mediated apoptosis in hepatocellular carcinoma Bel-7402 cells. Am J Chin Med 2015;43:137–48.
[49] Yu X, Zhou X, Fu C, Wang Q, Nie T, Zou F, et al. Celastrol induces apoptosis of human osteosarcoma cells via the mitochondrial apoptotic pathway. Oncol Rep 2015;34:1129–36.
[50] He T, Lin X. Theaflavin-3,3′-Digallate Plays a ROS-mediated dual role in ferroptosis and apoptosis via the MAPK pathway in human osteosarcoma cell lines and xenografts. Oxid Med Cell Longev 2022;2022:8966368.
[51] Jin H, Kim HS, Yu ST, Shin SR, Lee SH. Synergistic anticancer effect of docosahexaenoic acid and isoliquiritigenin on human colorectal cancer cells through ROS-mediated regulation of the JNK and cytochrome c release. Mol Biol Rep 2021;48:1171–80.
[52] Shi J, Li J, Xu Z, Chen L, Luo R, Zhang C, et al. Celastrol: a review of useful strategies overcoming its limitation in anticancer application. Front Pharmacol 2020;11:558741.
[53] Song J, He GN, Dai L. A comprehensive review on celastrol, triptolide and triptonide: insights on their pharmacological activity, toxicity, combination therapy, new dosage form and novel drug delivery routes. Biomed Pharmacother 2023;162:114705.
[54] Machado AR, Pinheiro AC, Vicente AA, Souza-Soares LA, Cerqueira MA. Liposomes loaded with phenolic extracts of Spirulina LEB-18: physicochemical characterization and behavior under simulated gastrointestinal conditions. Food Research Int 2019;120:656–67.
[55] Lavanya N, Muzib YI, Aukunuru J, Balekari U. Preparation and evaluation of a novel oral delivery system for low molecular weight heparin. Int J Pharm Investig 2016;6:148–57.
[56] Song T, Wang H, Liu Y, Cai R, Yang D, Xiong Y. TPGS-modified long-circulating liposomes loading Ziyuglycoside I for enhanced therapy of myelosuppression. Int J Nanomedicine 2021;16:6281–95.
[57] Zhang N, Yan F, Liang X, Wu M, Shen Y, Chen M, et al. Localized delivery of curcumin into brain with polysorbate 80-modified cerasomes by ultrasound-targeted microbubble destruction for improved Parkinson's disease therapy. Theranostics 2018;8:2264–77.
[58] Fu X, Zhang G, Liu R, Wei J, Zhang-Negrerie D, Jian X, et al. Mechanistic study of human glucose transport mediated by GLUT1. J Chem Inf Model 2016;56:517–26.
[59] Deng D, Xu C, Sun P, Wu J, Yan C, Hu M, et al. Crystal structure of the human glucose transporter GLUT1. Nature 2014;510:121–5.
[60] Cao S, Chen Y, Ren Y, Feng Y. GLUT1 biological function and inhibition: research advances. Future Med Chem 2021;13:1227–43.
[61] Freemerman AJ, Johnson AR, Sacks GN, Milner JJ, Kirk EL, Troester MA, et al. Metabolic reprogramming of macrophages: glucose transporter 1 (GLUT1)-mediated glucose metabolism drives a proinflammatory phenotype. J Biol Chem 2014;289:7884–96.
[62] Liu YH, Qin HY, Zhong YY, Li S, Wang HJ, Wang H, et al. Neutral polysaccharide from Panax notoginseng enhanced cyclophosphamide antitumor efficacy in hepatoma H22-bearing mice. BMC Cancer 2021;21:37.